RAA 2018 Vol. **18** No. **3**, 31(14pp) doi: 10.1088/1674–4527/18/3/31

http://www.raa-journal.org *http://iopscience.iop.org/raa*

***R**esearch in*
***A**stronomy and*
***A**strophysics*

Morphology of the ^{13}CO(3–2) millimetre emission across the gas disc surrounding the triple protostar GG Tau A using ALMA observations

Nguyen Thi Phuong[1,2,3], Pham Ngoc Diep[1,2], Anne Dutrey[3], Edwige Chapillon[3,4], Pierre Darriulat[1], Stéphane Guilloteau[3], Do Thi Hoai[1], Pham Tuyet Nhung[1], Ya-Wen Tang[5], Nguyen Thi Thao[1] and Pham Tuan-Anh[1]

[1] Department of Astrophysics, Vietnam National Space Center, Vietnam Academy of Science and Technology, Hanoi, Vietnam; *ntphuong02@vnsc.org.vn*
[2] Graduate University of Science and Technology, Vietnam Academy of Science and Technology, Hanoi, Vietnam
[3] Laboratoire d'Astrophysique de Bordeaux, Université de Bordeaux, CNRS, F-33615 Pessac
[4] IRAM, F-38406 Saint Martin d'Hères Cedex, France
[5] Academia Sinica, Institute of Astronomy and Astrophysics, Taipei

Received 2017 November 7; accepted 2017 December 29

Abstract Observations by the Atacama Large Millimetre/sub-millimetre Array of the dust continuum and ^{13}CO(3–2) millimetre emissions of the triple stellar system GG Tau A are analysed, giving evidence for a rotating gas disc and a concentric and coplanar dust ring. The present work complements an earlier analysis (Tang et al.) by exploring detailed properties of the gas disc. A 95% confidence level upper limit of 0.24″ (34 au) is placed on the disc scale height at a distance of 1″ (140 au) from the central stars. Evidence for Keplerian rotation of the gas disc is presented, with the rotation velocity reaching ∼3.1 km s^{-1} at 1″ from the central stars, and a 99% confidence level upper limit of 9% is placed on relative contribution from a possible in-fall velocity. Variations of the intensity across the disc area are studied in detail and confirm the presence of a hot spot in the south-eastern quadrant. However several other significant intensity variations, in particular a depression in the northern direction, are also revealed. Variations of the intensity are found to be positively correlated to variations of the line width. Possible contributions to the measured line width are reviewed, suggesting an increase of the disc temperature and opacity with decreasing distance from the stars.

Key words: protoplanetary disks — stars: low-mass — stars: individual (GG Tau A)

1 INTRODUCTION

GG Tau A is a triple stellar system, 1 to 5 million years old, located at 140 pc in a hole in the Taurus-Auriga star forming region. The separation between the main star GG Tau Aa and the close binary GG Tau Ab (Ab1-Ab2) is 35 au while the separation between GG Tau Ab1 and Ab2 is only 4.5 au (Di Folco et al. 2014). GG Tau A is surrounded by an envelope of gas and dust with a ring extending from ∼180 to 260 au and an outer disc extending up to ∼800 au from the central stars with an estimated mass of ∼0.15 solar masses (Dutrey et al. 1994). There is neither known molecular outflow nor jets associated with GG Tau A. Additional information about the system can be found in the review by Dutrey et al. (2016) and from references therein. In particular, high resolution Atacama Large Millimetre/sub-millimetre Array (ALMA) observations of ^{12}CO(6–5) emission and underlying continuum (Dutrey et al. 2014) have suggested possible planet formation. The present article uses ALMA data of the ^{13}CO(3–2) emission and underlying continuum that have been presented earlier by Tang et al. (2016) together with ^{12}CO(3–2) observations. Contrary to ^{12}CO(3–2) emission, which extends down to small distances from the

central stars, ^{13}CO(3–2) emission is limited to an outer ring having an inner edge radius of $\sim 1''$. The present analysis aims at complementing that of Tang et al. (2016) by providing new detailed information on the properties of the gas disc.

2 OBSERVATIONS AND DATA REDUCTION

The observations used in the present article were made in cycle 1 of ALMA operation (2012.1.00129.S) on 2013 November 18 and 19 in three blocks (Tang et al. 2016). The time spent on source was 1.84 hours. The number of antennas was 28, with the longest baseline being 1284.3 m. The three blocks of continuum data have been merged and calibrated by the ALMA staff and the ^{13}CO(3–2) data have been calibrated using CASA[1] and GILDAS[2]. The origin of coordinates at RA=$4^{\rm h}32^{\rm m}30.3^{\rm s}$ and DEC=$17^\circ\,31'\,40''$ corresponds to year 2000. Between 2000 and the time of observation, the source has moved by $0.24''$ east and $0.26''$ south (proper motion of [17, -19] mas per year taken from the SIMBAD[3] database); the data have been corrected accordingly.

The continuum emission was observed at $\sim$0.9 mm wavelength over frequencies covering from 330.655 to 344.426 GHz. The beam size (full width at half maximum, FWHM) is 0.39×0.29 arcsec^2 with a position angle (measured from north to east) of 56°. The ^{13}CO(3–2) emission was self-calibrated. The beam size (FWHM) is 0.37×0.31 arcsec^2 with a position angle of 80°. The present analysis is performed in the image plane and we evaluate the uncertainty on position measurements due to noise to be typically below $0.01''$, depending on the signal to noise ratio. However, it is often dominated by systematics and needs to be evaluated for each case separately. The spectral resolution (channel) has been smoothed to 0.11 km s^{-1} and the Doppler velocity covers between -2 and 15 km s^{-1}. Here, Doppler velocities are defined as the difference between the measured velocity and a systemic velocity of 6.38 ± 0.02 km s^{-1} as used by Dutrey et al. (2014) for ^{12}CO(6–5) about which the profile is symmetric.

[1] *http://casa.nrao.edu*

[2] *https://www.iram.fr/IRAMFR/GILDAS*

[3] *http://simbad.harvard.edu/simbad/sim-fbasic*

3 GENERAL FEATURES

3.1 Continuum Data

Figure 1 (left) maps the brightness of the continuum emission. It shows an elliptical ring surrounding a central source. The right panels show the projections on the x (right ascension offset) and y (declination offset) axes of the central source intensity integrated over y and x respectively. Gaussian fits give mean values of $0.06''$ and $-0.13''$ and FWHM values of $0.40''$ and $0.33''$ in x and y respectively, similar to the beam size: the central source is unresolved.

Figure 2 (left) displays the x and y projections of the continuum brightness integrated over y and x respectively. It requires the distance $R' = \sqrt{(x-0.06)^2 + (y+0.13)^2}$ to the central source to exceed $0.5''$, thereby excluding its contribution. The corresponding mean values of x and y are $-0.05''$ and $-0.09''$ respectively, showing that the ring is shifted north-west by $\sim$0.12$''$ with respect to the central source. The position and width measurements illustrated in Figure 1 and Figure 2 are accurate to better than $0.02''$, using the residuals of the fits to estimate measurement errors. They are dominated by systematics rather than simply by thermal noise. However, the angular separation between GG Tau Aa and Ab is $0.25''$: depending on what is being talked about, the position of the "centre" may vary by some $\pm 0.1''$.

Figure 2 (right) displays the dependence on $R = \sqrt{x^2+y^2}$ of the continuum brightness averaged over position angle $\varphi = 90^\circ - \tan^{-1}(y/x)$ (measured from north to east), again excluding the central source by requiring $R' > 0.5''$. A Gaussian fit to the peak gives a mean of $1.445'' \pm 0.015''$ and a σ of $0.266'' \pm 0.015''$ depending on the interval of R over which the fit is performed. Retaining a σ value of $0.266''$ and subtracting the beam size in quadrature gives a de-convolved FWHM of $0.528'' \pm 0.035''$. Tang et al. (2016) quote a value of $0.54''$ for the de-projected and de-convolved width of a uniform ring. The effect of de-projection is negligible and the correction factor for Gaussian to square box fit is $\sqrt{2\pi}/2\sqrt{2\ln 2} = 1.06$, bringing the Tang et al. (2016) value down to $0.51''$ to be compared with the present result of $0.528'' \pm 0.035''$. This is a very good agreement given that the ring is neither uniform nor perfectly Gaussian and that possible wings of faint emission be-

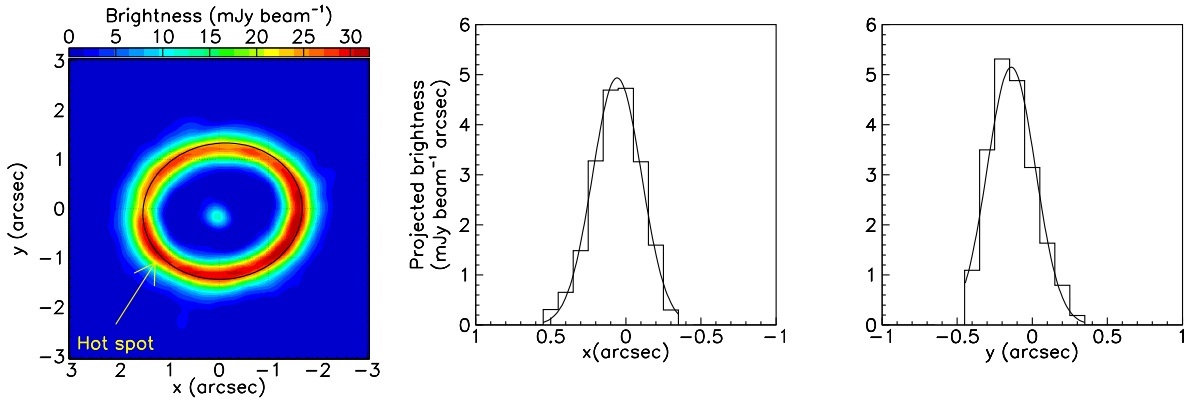

Fig. 1 Brightness of the dust ring continuum emission. *Left*: sky map; the *black ellipse* is the fit to $\langle R \rangle$ shown in Fig. 3; the *yellow arrow* points to the region of the hot spot observed by Dutrey et al. (2014) and Tang et al. (2016) in ^{12}CO(6–5) and ^{12}CO(3–2) emissions respectively. *Middle and right*: projections on the x and y axes of the central source brightness integrated over y and x respectively. The *lines* show Gaussian best fits.

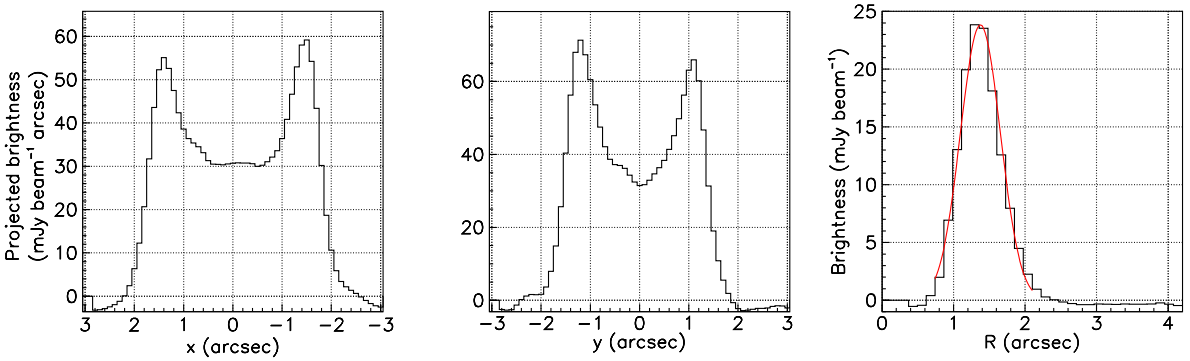

Fig. 2 Continuum brightness of the dust ring emission projected on the x (*left*) and y (*middle*) axes and integrated over y and x respectively. The *right panel* shows its distribution as a function of R, averaged over φ, together with the Gaussian best fit to the peak. In all three panels pixels having $R' < 0.5''$ are excluded.

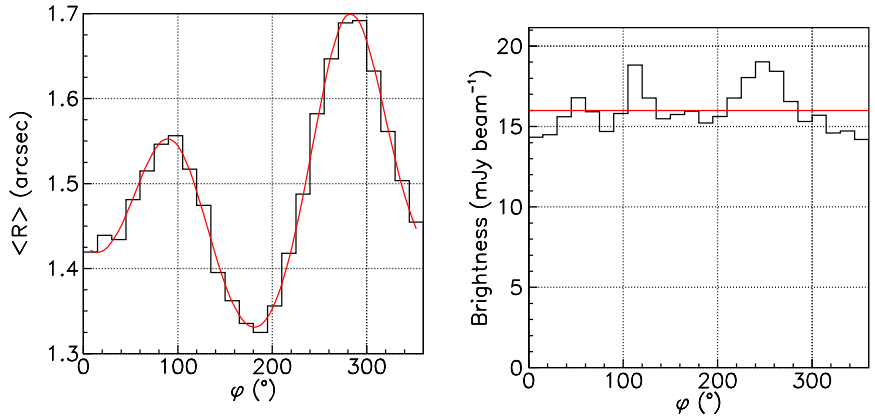

Fig. 3 Continuum emission. *Left:* Dependence on φ of $\langle R \rangle$ calculated in the interval $1'' < R < 2''$. The *red line* is the best fit to an elliptical tilted ring offset from the origin (see text). *Right:* Dependence on φ of the disc plane continuum brightness averaged over R in the interval $1'' < R < 2''$. The *red line* shows the mean value.

yond $1.8''$ would affect differently the two fitting procedures.

Figure 3 (left) displays the mean value of R, $\langle R\rangle$, weighted by the radial average of the brightness across the ring over the interval $1'' < R < 2''$. A fit of the dependence of $\langle R\rangle$ on φ as an ellipse of semi-major and semi-minor axes a_0 and b_0 respectively and offset by Δx and Δy has been made to first order in the offsets and in the ellipticity:

$$r = \Big(\frac{\cos^2(\varphi-\varphi_0)}{a_0^2} - 2\frac{\Delta x}{\sqrt{a_0 b_0}}\frac{\cos(\varphi-\varphi_0)}{a_0^2} + \frac{\sin^2(\varphi-\varphi_0)}{b_0^2} - 2\frac{\Delta y}{\sqrt{a_0 b_0}}\frac{\sin(\varphi-\varphi_0)}{b_0^2}\Big)^{-1/2}. \quad (1)$$

It gives $a_0 = 1.62''$ and $b_0 = 1.38''$, position angle of the major axis $\varphi_0 = 97^\circ$ and small offsets $\Delta x = -0.07''$ and $\Delta y = -0.05''$, at the level of measurement uncertainties. This confirms the good centering of the ring on the origin of coordinates and the aspect ratio corresponds to a tilt with respect to the sky plane $\theta = \cos^{-1}(1.38/1.62) = 32^\circ \pm 4^\circ$ of a circular ring about the rotated (by 7.0°) x axis.

These results confirm the values quoted by Tang et al. (2016): $1.63''$ instead of $1.62''$ for a_0, 7.5° instead of 7.0° for the position angle and 36.4° instead of 32° for the tilt with respect to the sky plane, with the latter being measured to no better than $\pm 4^\circ$. The values quoted for the tilt by Dutrey et al. (2014) are $37^\circ \pm 1^\circ$ for ^{12}CO(6–5) and $35.0^\circ \pm 0.2^\circ$ for the dust.

Figure 3 (right) displays the dependence on position angle φ of the continuum brightness averaged over R in the interval $1'' < R < 2''$. Here we have used the fact that the ratio between the beam area in the sky plane and its de-projected value in the disc plane is equal to $\langle R\rangle / a_0$. In the disc plane the brightness is uniform over the disc circumference and equal to $16.0\,\mathrm{mJy\,beam^{-1}}$ to within $\pm 8.5\%$ (rms).

3.2 ^{13}CO(3–2) Line Emission

Figure 4 (left) displays the brightness distribution over the data cube. A Gaussian fit to the noise peak gives a mean of $-0.19\,\mathrm{mJy\,beam^{-1}}$ and a σ of $7.2\,\mathrm{mJy\,beam^{-1}}$ (0.56 K). Figure 4 (right) displays the Doppler velocity (V_z) spectrum integrated over 8×8 arcsec^2, with a double-horn profile typical of a rotating volume. It is centred to better than $0.1\,\mathrm{km\,s^{-1}}$. In what follows, throughout the article, we restrict the Doppler velocity range to $|V_z| < 2\,\mathrm{km\,s^{-1}}$ unless specified otherwise.

Figure 5 displays the sky maps of the velocity-integrated brightness, or integrated intensity, and of the mean Doppler velocity. The map of the integrated intensity shows a clear ring of gas surrounding the central stars and having morphology similar to the dust morphology, indicating a concentric circular gas disc having the same inclination as the dust ring on the sky plane. It displays no central emission, with an abrupt inner cut-off at $\sim 1''$; there is no significant emission inside an ellipse scaled down from the dust ellipse by a factor $\sim$3, meaning a de-projected radius of $\sim 1.62/3 = 0.54''$. The velocity map excludes the region inside the scaled-down ellipse where noise dominates. It displays a clear velocity gradient along the major axis of the ellipse, as expected from rotation of the tilted disc about its axis. Note that an infalling (rather than rotating) disc would display instead a gradient along the minor axis of the ellipse. In general adding some in-fall motion to rotation would cause the axis of the velocity gradient to deviate from the major axis, the more so the larger the relative contribution of in-fall.

Figure 6 is the equivalent for the line of Figure 2 for the continuum except that Figure 2 is for the continuum and Figure 6 is for the line: projections on the x and y axes and r-dependence, averaged over φ, of the integrated intensity, where r is now the de-projected value of R in the disc plane (see Fig. 8). Here, de-projection assumes a tilt angle of 32° and a position angle of the disc axis of 7°, as found for the dust. In all panels we exclude the central region where noise dominates by requiring $r > 0.54''$. When compared with the dust (continuum) ring, the gas (line) ring is broader and peaks at smaller radii. The mean values of x and y are $0.02''$ and $-0.10''$ respectively. A fit to the integrated intensity distribution as a function of r as a sum of three Gaussians is shown in the right panel of the figure. The means and widths of the Gaussians are fixed to the values obtained by Tang et al. (2016) when fitting the western half of the gas disc.

Figure 7 (left) displays the mean value of R, $\langle R\rangle$, weighted by the radial average of the brightness across the ring over the interval $0.54'' < r < 2''$. A fit of the dependence of $\langle R\rangle$ on φ as an ellipse gives semi-major and semi-minor axes $a_0 = 1.45''$ and $b_0 = 1.19''$ respectively, position angle of the major axis $\varphi_0 = 97.8^\circ$ and small offsets $\Delta x = 0.02$ and $\Delta y = 0.07''$. The position

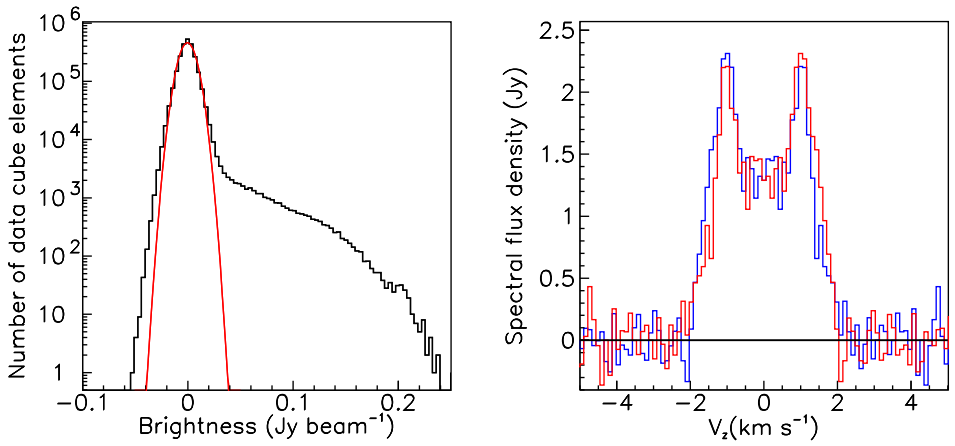

Fig. 4 *Left:* Line brightness distribution (Jy beam^{-1}); the *red curve* is a Gaussian fit to the noise peak. *Right:* Doppler velocity spectrum weighted by brightness and integrated over 8×8 arcsec^2 (*blue*); the *red histogram* is obtained from the original by symmetry about the origin.

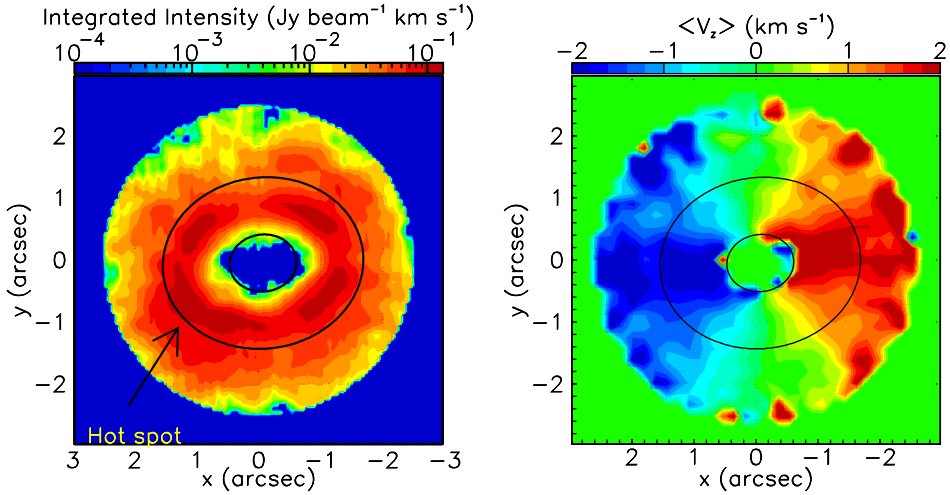

Fig. 5 *Left:* Sky map of the ^{13}CO(3–2) integrated intensity. The *black arrow* shows the position of the hot spot in ^{12}CO(6–5) (Dutrey et al. 2014) and ^{12}CO(3–2) (Tang et al. 2016). *Right:* Sky map of the mean Doppler velocity (weighted by brightness) excluding the region contained in the scaled-down ellipse shown in the *left panel*. In both panels, $R < 2.5''$ and the *black ellipses* are the best fits to the distribution of $\langle R \rangle$ in the continuum data and its scaled-down version (by a factor 3).

angle and aspect ratio (0.82 instead of 0.85) are very similar to the dust result, but the size of the ellipse is scaled down by a factor 87%. The tilt angle is now 35°, compared with 32° for the dust.

Another estimate of the tilt geometry is obtained from the map of the mean Doppler velocity (Fig. 7, middle). In a ring defined as $0.54'' < r < 2''$, a fit of the form $\langle V_z \rangle = V_0 - \Delta V \cos(\varphi - \varphi_0)$ gives $V_0 = 0.05\,\mathrm{km\,s^{-1}}$, $\Delta V = 1.73\,\mathrm{km\,s^{-1}}$ and $\varphi_0 = 97.8°$, again in excellent agreement with the value obtained from the dust fit, $\varphi_0 = 97.0°$; this provides evidence against a significant in-fall contribution. The values quoted by Dutrey et al. (2014) are $97° \pm 2°$ for ^{12}CO(6–5) and $96.5° \pm 0.2°$ for the dust. The value of ΔV, $1.73\,\mathrm{km\,s^{-1}}$, corresponds to a mean rotation velocity of $\sim \Delta V / \sin\theta \sim 3.3\,\mathrm{km\,s^{-1}}$.

Figure 7 (right) displays the dependence on φ of the disc plane integrated intensity averaged across the ring in the interval $0.54'' < r < 2''$. It has a mean value of 0.39 Jy beam^{-1} km s^{-1} and fluctuates around it with an rms of 17%. We summarise the geometry parameters of the dust and ^{13}CO(3–2) emission in Table 1.

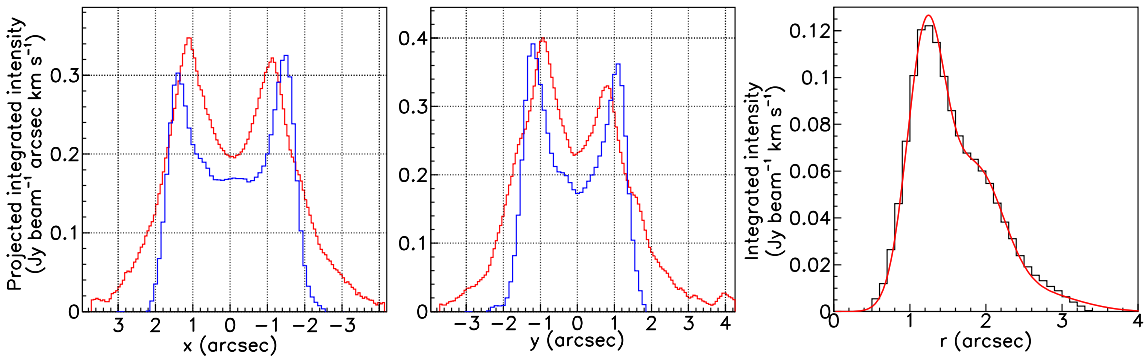

Fig. 6 Line emission. *Left* and *middle:* Continuum brightness (*blue*, arbitrary normalisation) and line integrated intensity (*red*) projected on the x (*left*) and y (*middle*) axes in the region of $r > 0.5''$. *Right:* r-dependence, averaged over φ, of the integrated intensity in the disc plane. The *red line* is a fit using the same three Gaussians as in Tang et al. (2016).

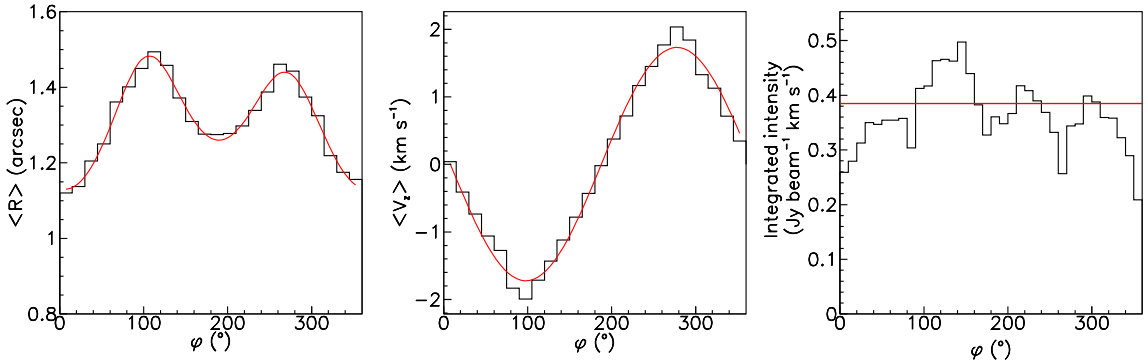

Fig. 7 Line emission. *Left:* Mean value of R, $\langle R\rangle$, weighted by the radial average of the brightness across the disc over the interval $0.54'' < r < 2''$. The *red line* is the result of the fit described in the text. *Middle:* Dependence on φ of the mean line Doppler velocity (brightness-weighted); the *red line* is the result of the fit described in the text. *Right:* Dependence on φ of the disc plane integrated intensity averaged across the disc ($0.54'' < r < 2''$). The *red line* shows the mean value.

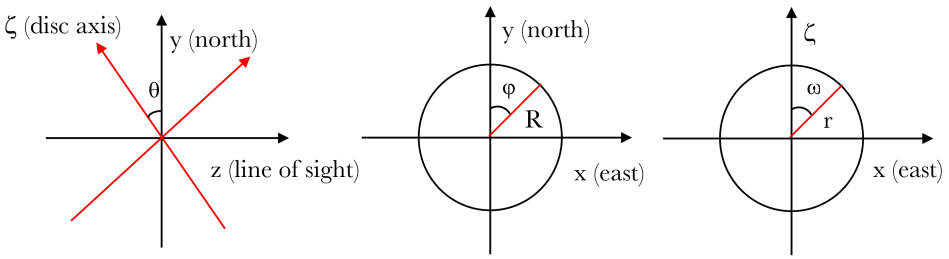

Fig. 8 Geometry. *Left*: in the (y, z) plane; *middle*: in the sky plane (x, y); *right*: in the disc plane (x, ζ).

4 DETAILED PROPERTIES OF THE GAS DISC

In the present section we use new coordinates obtained from those of the preceding sections by a rotation of an angle of 8° about the z axis. To within 1°, this brings the new x axis on the major axes of the ellipses found in the preceding sections as best describing the φ dependences of both $\langle R\rangle$ and the Doppler velocity. Moreover, unless otherwise explicitly specified, we assume a tilt of $\theta = 35°$ for the disc plane as a reasonable compromise between values obtained in both earlier and the present studies, for both gas and dust observations. In practice, we use 99×81 pixels of 0.06×0.06 arcsec^2 on the sky

Table 1 Geometry Parameters

		Projection on x and y		Ellipse fitted to the $\langle R\rangle$ vs φ					
		$\langle x\rangle$ ($''$)	$\langle y\rangle$ ($''$)	a_0 ($''$)	b_0 ($''$)	φ_0 ($^\circ$)	Δx ($''$)	Δy ($''$)	θ ($^\circ$)
Dust	Central source	0.06	-0.13	-	-	-	-	-	-
	Ring	-0.05	-0.09	1.62	1.38	97.0	-0.07	-0.05	32
^{13}CO(3–2)	Disc	0.02	-0.01	1.45	1.19	97.8	0.02	0.07	35

map, covering $(99\times0.06)\times(81\times0.0733)\sim6\times6$ arcsec^2 in the disc plane ($0.0733 = 0.06/\cos35^\circ$). To each pixel (x, y) we associate disc coordinates $\zeta = y/\cos\theta$, $r = \sqrt{x^2+\zeta^2}$ and $\omega = 90^\circ - \tan^{-1}(\zeta/x)$. Here "disc plane" and "disc coordinates" are simply defined by this transformation, implying no assumption on the disc being actually thin and flat.

4.1 Estimate of the Disc Thickness Obtained from the Sharpness of the Disc Inner Edge

Tang et al. (2016) have commented on the sharpness of the inner edge of the ^{13}CO(3–2) emission and on the smallness of the vertical temperature gradient, with the inner edge of the disc being directly exposed to stellar light and casting a shadow on the outer disc. Here, we compare the value of the smearing of the inner edge of the disc map near the major axis of the ellipse with its value near the minor axis. To a good approximation, the effect of disc thickness essentially cancels for the former while, for the latter, it scales with the product of disc thickness by sine of the tilt angle. The optical thickness of the line is not expected to strongly affect this result. We consider four angular sectors in the disc plane, each 60° wide and centred on the axes of the ellipse. In each sector, we study the radial dependence of the integrated intensity, both in the disc plane (r) and in the sky plane (R). The result is displayed in Figure 9. In order to evaluate the sharpness of the inner edge of the gas disc, we fit a Gaussian to the rise of each distribution, between $0.5''$ and $1.5''$ in r. In R, we use the same interval of $0.5''$ to $1.5''$ for the sectors centred on the major axis of the ellipse but a scaled-down (by a factor $\cos35^\circ = 0.82$) interval of $0.41''$ to $1.23''$ for the sectors centred on the minor axes in order to account for the effect of tilt. The mean and σ values (dispersions, a factor 2.35 smaller than FWHM values also commonly quoted in the literature) obtained for the Gaussian best fits are listed in Table 2.

The distributions as a function of r show identical σ values, to within ±10 mas, in the four angular sectors. A contribution from the disc thickness would cause these values to be larger in the minor-axis sectors than in the major-axis sectors: it is already clear that a significant contribution from the disc thickness is excluded. At variance with the distributions as a function of r, the distributions as a function of R show significantly different σ values for the major-axis sectors, $\sim0.33''$, and the minor-axis sectors, $\sim0.28''$, a factor 85% smaller. Similarly, the ratio between the mean values of the Gaussians (listed as "scaling factor" in the table) are equal for the two sectors of a same axis of the ellipse, but again 85% smaller for sectors centred on the minor axis than for those centred on the major axis. The latter are very slightly smaller than unity, as expected from the 60° angular widths of the sectors. The consistency between these numbers suggests an interpretation of the σ values measured in the R distributions as the sum of three terms added in quadrature: i) a beam contribution of $0.14''$ on both the minor- and major-axis sectors (calculated from the known beam parameters); ii) a contribution from the intrinsic smearing of the disc emission, σ_0, caused by effects such as density variations and contributing in each sector a value σ_0 scaled down by the scaling factors listed in the table; iii) an additional contribution σ_1 due to the disc thickness and contributing only to the minor-axis sectors. After subtraction of the beam contribution and correction for de-projection, one obtains values for σ of $0.29''$ for the minor-axis sectors and $\sim0.30''$ for the major-axis sectors. A contribution σ_1 due to the disc thickness would cause the former to exceed the latter, at variance with what is observed. From the consistency between the numbers, we estimate an uncertainty of $\sim0.02''$ on the Gaussian σs. To a 95% confidence level (2σ) we obtain an upper limit for σ_1 of $\sqrt{(0.29+2\times0.02)^2-0.30^2}$=$0.14''$, corresponding to a scale height $H(r) \sim 0.14/\sin35^\circ = 0.24''$ (34 au)

Table 2 Estimating the thickness of the gas disc from the sharpness of its inner edge projected on the sky plane. All values (except the scaling factors) are in arcsec.

		North	East	South	West
r fit	$\langle r \rangle$	1.15	1.31	1.24	1.34
	σ	0.32	0.34	0.33	0.32
R fit	$\langle R \rangle$	0.99	1.29	1.08	1.32
	σ	0.28	0.34	0.28	0.32
R fit, beam subtracted	σ	0.24	0.31	0.24	0.29
R fit, de-projected	Scaling factor	0.86	0.98	0.87	0.99
	σ	0.29	0.31	0.29	0.29

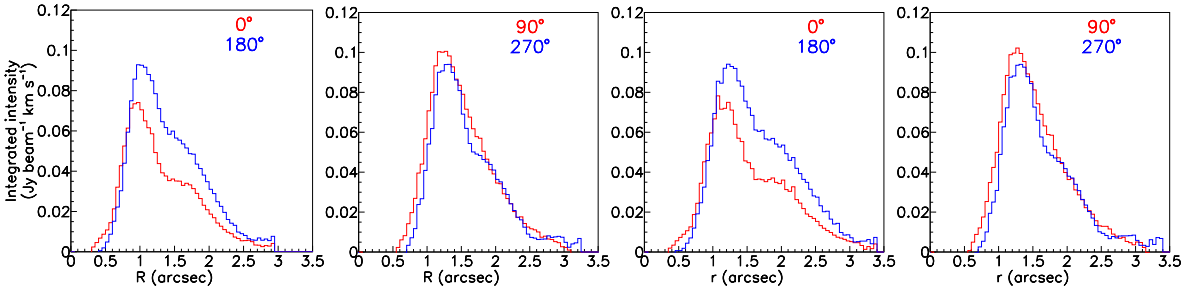

Fig. 9 Line emission. Dependence on R (*left panels*) and on r (*right panels*) of the line integrated intensity averaged in 60° wide angular sectors centred on the ellipse axes. In each case, the *leftmost panel* is for minor-axis sectors and the *rightmost panel* for major-axis sectors. The central values of ω are indicated in the inserts for each sector.

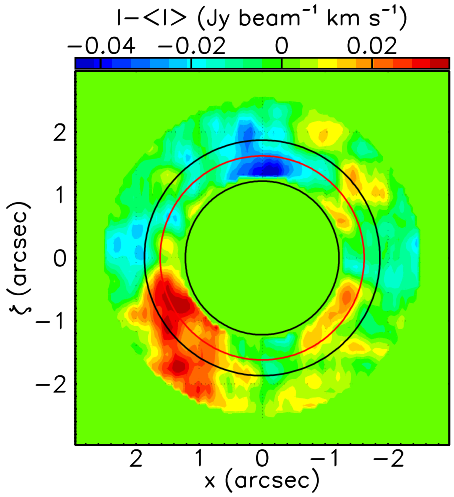

Fig. 10 Line emission. Map in the disc plane of the difference between the integrated intensity and its value averaged over ω at the same r. The *black circles* show the maxima of the Gaussians describing the mean radial integrated intensity distribution, $r = 1.22''$ and $1.87''$ respectively. The *red circle* corresponds to the mean value of r in the dust map ($1.62''$).

at $r \sim 1''$ (140 au) where the Keplerian velocity is $\sim 3\,\mathrm{km\,s^{-1}}$; at 30 K, the sound velocity is $\sim 0.5\,\mathrm{km\,s^{-1}}$ and hydrostatic equilibrium implies $H(r) = 0.5/3 = 0.17''$ compared with the $0.24''$ upper limit obtained above. We have checked that this result is independent of the width of the angular sectors (using 40° instead of 60° lowers the Gaussian σs by $\sim 0.01''$). Depending on the interval chosen for calculation, the Gaussian σ's lower values of the σ_1 upper limit may be obtained, as low as $0.10''$ instead of $0.14''$. We conservatively prefer to retain the latter value as our final result.

4.2 Integrated Intensity Variations across the Disc

In order to better understand the nature of the integrated intensity variations displayed in Figure 7 (right), we display in Figure 10 the map in the disc plane of the difference between measured integrated intensity and its value averaged over ω at the same value of r (as obtained from Fig. 6, right). This map provides a measure of the lack of rotational symmetry of the integrated intensity in the disc plane. It gives strong evidence for an excess associated with the hot spot observed by Dutrey et al. (2014) and Tang et al. (2016) and for a northern depression of similar amplitude. Both excess and depression reach their maxima at a distance from the central stars corresponding to the gap between the maxima of the two first Gaussians describing the mean radial distribution of the integrated intensity (these Gaussians peak at $r = 1.22''$ and $1.87''$ respectively). It is also in this gap that the continuum dust emission peaks (at $r = 1.62''$). However, both excess and depression extend to larger values of r, particularly the former that extends out to $r \sim 2.5''$.

4.3 Gas Kinematics

Calling $V_{\rm rot}$ and $V_{\rm fall}$ the components of the disc plane velocity respectively perpendicular and parallel to the disc radius, the Doppler velocity reads $V_z = \sin\theta(V_{\rm rot}\sin\omega - V_{\rm fall}\cos\omega)$ for each data-cube element (x, y, V_z). To a good approximation, $V_{\rm fall}$ can be neglected and we can calculate $V_{\rm rot} = V_z(\sin\theta\sin\omega)^{-1}$ for each data-cube element, leaving for later the task of revealing a possible small $V_{\rm fall}$ contribution. $V_{\rm rot}$ becomes trivially singular along the ζ axis. We require accordingly $|\sin\omega|$ to exceed 0.3 when calculating $V_{\rm rot}$. As $\sin^{-1}(0.3) = 17.5°$, this is not much of a loss.

Figure 11 displays the dependence on ω and r of V_z averaged (using brightness as weight) over $0.8'' < r < 2.5''$ and over ω respectively. Averaging V_z requires some care in dealing with the noise: the interval used for averaging must be symmetric with respect to the mean value obtained as a result, which requires relaxing the condition $|V_z| < 2\,{\rm km\,s^{-1}}$ usually applied in the analysis. The ω-dependence is perfectly described by a sine wave of amplitude $-1.43\,{\rm km\,s^{-1}}$. Adding a cosine term does not change the coefficient of the sine term and insignificantly improves the value of χ^2. Its amplitude is $-0.05\,{\rm km\,s^{-1}}$, only 2.6% of the amplitude of the $\sin\omega$ term, corresponding to a shift of $-1.9°$ in ω. As a check of the correctness of the procedure, we compare this result with what is obtained when requiring a 3σ cut on each data-cube element; the amplitudes of the sine and cosine waves become -1.40 and $-0.04\,{\rm km\,s^{-1}}$ respectively.

The negative sign of the best-fit cosine term means radial expansion, and in-fall would give a positive sign. Assuming a 3° uncertainty on ω, corresponding to half a beam sigma at a distance of $1.3''$, we obtain a 3σ upper limit (99% confidence level) of 9% on the ratio $V_{\rm fall}/V_{\rm rot}$. As a function of r, averaging over ω would cause $\langle V_z\rangle$ to cancel if symmetry with respect to the ζ axis were perfect. It is indeed found to be very small, at the level of $-0.05\,{\rm km\,s^{-1}}$ as soon as r exceeds the peak of the radial integrated intensity distribution at $r \sim 1.3''$.

Similarly, the dependence on ω and r of $V_{\rm rot}$ averaged respectively (using brightness as weight) over $0.8'' < r < 2.5''$ and over ω ($|\sin\omega| > 0.3$) is displayed in Figure 12. The left panel shows the distribution of $\langle V_{\rm rot}\, r^{1/2}\rangle$ on r, which would be constant if the rotation were Keplerian. A fit in the interval $1.1'' < r < 2.5''$ gives a power index of -0.63 instead of the Keplerian -0.5 and $\langle V_{\rm rot}\rangle = 3.0\,{\rm km\,s^{-1}}$ at $r = 1''$. The middle panel illustrates the difficulty in measuring $V_{\rm rot}$ reliably due to its singularity on the ζ axis. As remarked earlier, the binarity of the central star prevents the position of the "centre" from being defined to better than some $\pm0.1''$ (more exactly such a definition requires modelling properly the binary configuration). Shifting the origins of x and y on the sky map by ±1 pixel size ($\pm0.06''$) changes the value of ω and therefore of $V_{\rm rot}$. The result displayed in the middle panel shows the importance of the effect. As a result, increasing the $|\sin\omega|$ cut from 0.3 to 0.707 ($\sin 45°$) makes the $\langle V_{\rm rot}\, r^{1/2}\rangle$ distribution Keplerian with a power index of -0.51 instead of -0.63, and the rotation velocity at $r = 1''$ increases from 3.0 to $3.1\,{\rm km\,s^{-1}}$ (left panel). We display, in the right panel, the map of $V_{\rm rot}\, r^{1/2}$ in the disc plane. It is uniform except for increases near the ω limits in the north-west and south-east directions. These are largely artefacts due to the difficulty in calculating a reliable $V_{\rm rot}$ near the ζ axis. Note that Dutrey et al. (2014) quote a $V_{\rm rot}$ value of $3.4 \pm 0.1\,{\rm km\,s^{-1}}$ for ^{12}CO(6–5) emission with an index of -0.5 ± 0.1 at $r = 100\,{\rm au}$; this corresponds to $2.9\,{\rm km\,s^{-1}}$ at $r = 1''$, consistent with the $3.0\,{\rm km\,s^{-1}}$ observed here for ^{13}CO(3–2) emission.

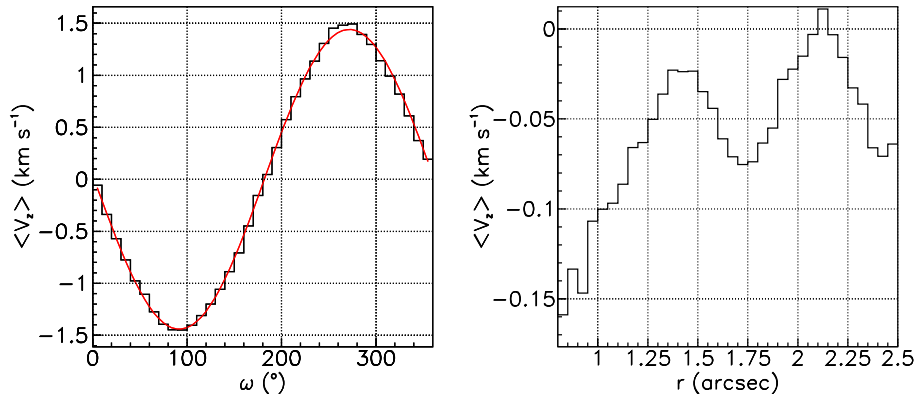

Fig. 11 Distributions on ω (*left*) and r (*right*) of the Doppler velocity respectively averaged over $0.8'' < r < 3.2''$ and over ω. In the *left panel*, the *line* shows the best fit result of the form $-1.43 \sin\omega + 0.05 \cos\omega = -1.43 \sin(\omega - 1.9°)\,\mathrm{km\,s^{-1}}$.

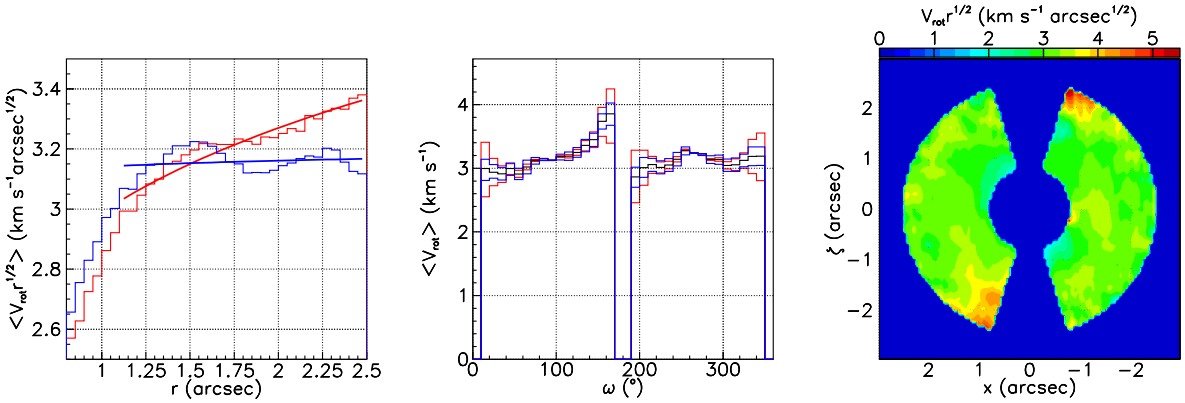

Fig. 12 *Left:* Dependence on r of $\langle V_{\rm rot}\, r^{1/2}\rangle$ (brightness-weighted average); the *lines* are the best power law fits with indices -0.63 for $|\sin\omega| > 0.3$ (*red*) and -0.51 for $|\sin\omega| > 0.707$ (*blue*). *Middle:* Dependence on ω of $\langle V_{\rm rot}\rangle$ (averaged in the interval $0.8'' < r < 2.5''$) calculated using the nominal origin of coordinates on the sky plane (*black histogram*) or by shifting the origin by $\pm 0.06''$ in either x or y (*red* and *blue histograms* respectively). *Right:* De-projected map of $\langle V_{\rm rot}\, r^{1/2}\rangle$ ($|\sin\omega| > 0.3$).

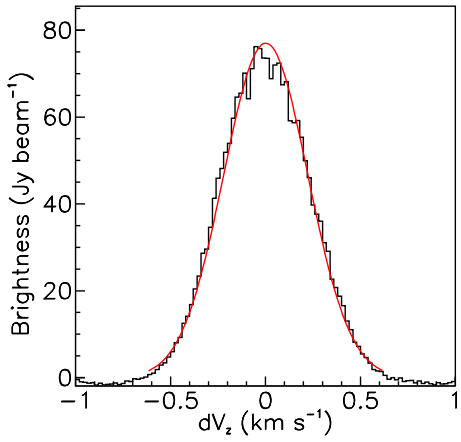

Fig. 13 Dependence of the brightness on the difference dV_z between measured values of V_z and their mean value in the associated pixel. Summing is over all pixels in the interval $0.8'' < r < 2.5''$. The curve is a Gaussian fit.

4.4 Line Width

Figure 13 displays the dependence of the brightness on the difference dV_z between the values of V_z measured in a given pixel and their mean values in that same pixel. The mean is calculated using brightness as a weight and the histogram is summed over all pixels in the interval $0.8'' < r < 2.5''$. A Gaussian fit gives a σ-value of $0.23\,\mathrm{km\,s^{-1}}$.

Several quantities, added in quadrature, are expected to contribute to σ_{vz}: Keplerian shear σ_K associated with both beam size and disc thickness, the instrumental resolution σ_I and the thermal broadening σ_T, possibly including a turbulence contribution (Teague et al. 2016), and opacity broadening, σ_τ.

Averaged over ω, the Keplerian shear at $r = 1.5''$ reads, from the derivative of a power law, $\sigma_K = 0.6\,\langle|V_z|\rangle\,\sigma_r/r$ where 0.6 stands for the power index of the radial $V_{\rm rot}$ distribution (it would be 0.5 in a pure Keplerian case). Here, σ_r is the sum in quadrature of the σs of the beam, $0.21''$, and of the disc thickness multiplied by $\tan\theta = 0.7$, $0.11''$. Hence, $\sigma_r \sim \sqrt{0.21^2 + 0.11^2} = 0.24''$ and $\sigma_K = 0.6 \times \sin(35^\circ) \times 3.1 \times 1.5^{-0.6} \times (2/\pi) \times\sigma_r/1.5 = 0.09\,\mathrm{km\,s^{-1}}$. Taking the FWHM of the instrumental resolution as one velocity bin gives $\sigma_I \sim 0.05\,\mathrm{km\,s^{-1}}$. Thermal broadening proper reads $\sqrt{2kT/M_{\rm co}}$ where k is Boltzmann constant, T the temperature and $M_{\rm co}$ the mass of the ^{13}CO molecule; at $T = 18\,\mathrm{K}$ (Tang et al. 2016) it amounts again to some $0.10\,\mathrm{km\,s^{-1}}$. Opacity tends to flatten the line profile and its effect is an effective broadening of $\sim \sqrt{\ln(\tau)}$, where τ is the line opacity (Piétu et al. 2007). Tang et al. (2016) show that ^{13}CO(3–2) and ^{12}CO(3–2) have similar brightness, implying that $\tau(^{13}\mathrm{CO})$ is significantly above unity. Using both ^{13}CO(3–2) and ^{12}CO(3–2), we estimate its value to be $\tau \sim 10$, meaning an effective broadening of $\sim$1.5 and a joint contribution of $\sim 0.15\,\mathrm{km\,s^{-1}}$ for thermal and opacity broadening. A possible additional source of broadening could be the effect of noise. However, using a 3σ cut to select the data, which must underestimate the measured value of σ_{vz}, we obtain 0.20 instead of $0.23\,\mathrm{km\,s^{-1}}$, showing that noise can be neglected within our estimated uncertainty of $\pm 0.03\,\mathrm{km\,s^{-1}}$.

Adding the estimated contributions in quadrature gives a total contribution of $\sqrt{0.05^2 + 0.09^2 + 0.15^2} = 0.18\,\mathrm{km\,s^{-1}}$ compared with $0.23 \pm 0.03\,\mathrm{km\,s^{-1}}$ measured: there is not much room left for additional contributions and turbulence is small (highly subsonic) in this disc.

Important additional information on the line width can be obtained from a study of the variations of σ_{vz} over the disc plane. To this end we consider three r intervals, $0.4''$ wide, covering between $1.3''$ and $2.5''$ and 24 ω-intervals, 15° wide, covering between 0° and 360°. The dependence on ω of the integrated intensity is shown in Figure 14 (left) for each r-interval separately. The hot spot sticks out at values of ω that increase from $\sim 120^\circ$ in the low r-interval to $\sim 150^\circ$ in the high r-interval. The middle panel shows the dependence on ω of the normalized value of V_z averaged in each r-ω bin separately; more precisely a fit of the form $\langle V_z\rangle = -a\,\sin\omega - b\cos\omega$ is performed in each r-ω bin separately and the normalization is made by dividing each of the three distributions by the corresponding value of a (respectively 1.46, 1.27 and $1.18\,\mathrm{km\,s^{-1}}$, namely $\sim 1.78\,\mathrm{km\,s^{-1}}$ divided by $\langle r\rangle^{1/2}$). The values of b are between 0.02 and $0.03\,\mathrm{km\,s^{-1}}$ and can be neglected. All three normalized histograms are described well by a sine wave. The right panel displays the dependence on ω of σ_{vz}: in each r-ω interval the σ of a Gaussian fit to the peak of the Doppler velocity spectrum is plotted after normalization to its value averaged over ω in the corresponding r-interval (0.258, 0.210, and $0.181\,\mathrm{km\,s^{-1}}$ respectively).

As a function of ω, the line width fluctuates relatively less than the integrated intensity. Moreover, there is no sign of a sine wave contribution that would signal the effect of Keplerian shear, confirming the conclusion that was reached above. While the hot spot dominates the variations of the integrated intensity, its presence is barely visible as an increase of the line width; conversely, sharper line width excesses at $\omega \sim 60^\circ$ and 320° are visible on the velocity-integrated distribution as less marked excesses. The depressions at $\omega \sim 0^\circ$, 90° and 270° are also associated with lower values of the line width. The correlation between σ_{vz} and fluctuations of the integrated intensity f is illustrated in Figure 15. In each (r, ω) bin we define $\Delta\sigma$ and Δf as the difference between the values of σ_{vz} and f and their mean in the r interval: $\Delta\sigma = \sigma_{vz}/\langle\sigma_{vz}\rangle - 1$ and $\Delta f = f/\langle f\rangle - 1$. A clear positive correlation is evidenced from the best linear fit, $\Delta\sigma = 0.32\,\Delta f$. Note that the correlation is even slightly stronger if one excludes the hot spot region, with the corresponding Pearson coefficients being respectively 0.25 and 0.32. From the low-r interval to the

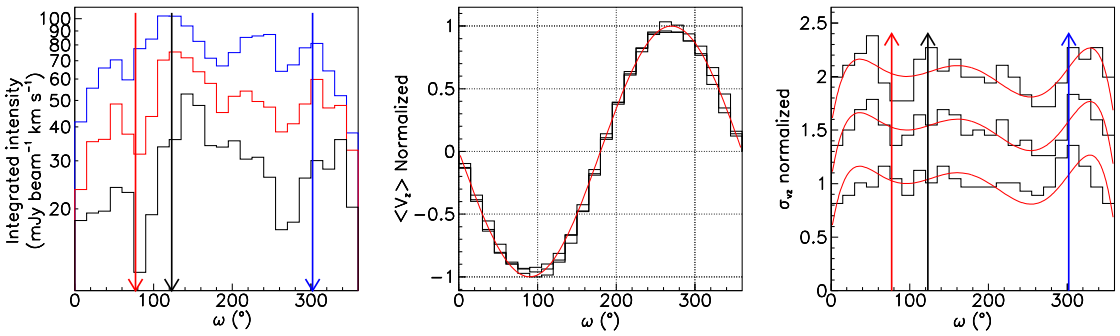

Fig. 14 *Left:* Dependence on ω of the integrated intensity for $1.3'' < r < 1.7''$ (*blue*), $1.7'' < r < 2.1''$ (*red*) and $2.1'' < r < 2.5''$ (*black*); *Middle:* dependence on ω of the value of $\langle V_z \rangle$ in each of the three r-intervals (*black histograms*); here, $\langle V_z \rangle$ has been divided by 1.46, 1.27 and 1.18 km s^{-1} respectively, making the three histograms nearly identical; the *red curve* is a sine wave. *Right:* dependence of σ_{vz} on ω, for each r-interval separately; in each r-ω bin, a Gaussian fit is performed to the peak of the V_z spectrum, giving a σ-value that averages to respectively 0.258, 0.210 and 0.181 km s^{-1}; the plotted histograms are normalized to these respective average values; in addition, for clarity, they are shifted up by respectively 0, 0.5 and 1. The *red curve*, a sixth degree polynomial fit to the distribution of the central r-interval, is shown to guide the eye. In the *left* and *right panels* the *arrows* point in the direction of increasing r and indicate remarkable features: the *black arrow* shows the hot spot as defined from the *left panel*; the *blue* and *red arrows* show peaks of the line width as defined from the *right panel*.

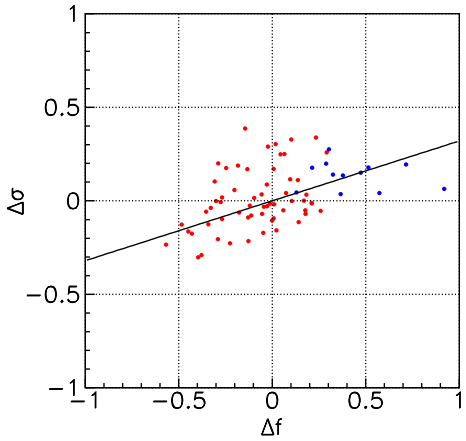

Fig. 15 Correlation between the normalized relative fluctuations of the line width $\Delta\,\sigma$ and the integrated intensity $\Delta\,f$ (see text). The *line* is the best fit to the data, $\Delta\,\sigma = 0.32\Delta\,f$. The *blue points* are for $105^\circ < \omega < 165^\circ$ (*hot spot*).

high-r interval the ω-averaged line width (σ) decreases by a factor 0.70 while the amplitude of the V_z sine wave decreases only by a factor 0.81. A possible explanation may be an increase of the temperature and opacity with decreasing r. An increase of temperature and opacity from (T, τ)=(18 K, 5) at $r \sim 2.3''$ to (36 K, 10) at $r \sim 1.5''$ would imply an effective thermal broadening increasing from ~ 0.13 km s^{-1} to about 0.21 km s^{-1}. Adding in quadrature σ_K and σ_I contributions of respectively 0.09 and 0.05 km s^{-1} would give respectively 0.15 and 0.23 km s^{-1}, compared with 0.18 and 0.26 km s^{-1} being measured.

The fact that the ω-dependence of $\langle V_z \rangle$ is very well described by a simple sine wave in each of the three intervals implies that the observations are consistent with $V_{\rm rot}$ being independent of ω. It shows again that the fluctuations of $V_{\rm rot}\, r^{1/2}$ observed in Figure 11 are affected by very large uncertainties. Indeed, very good fits to the measured V_z sky map are obtained by assuming a purely Keplerian rotation velocity. On the contrary, we estimate that the uncertainty attached to both $\langle V_z \rangle$ and σ_{vz} is of the order of only 0.02 km s^{-1}, making the discussion of the line width in terms of σ_{vz} more reliable than in terms of $V_{\rm rot}$ dispersion.

5 SUMMARY

In summary, the present analysis confirms the results obtained earlier by Tang et al. (2016). It reveals the presence of concentric dust and gas rings sharing the same axis projecting on the sky plane $\sim 7^\circ$ east of north. In the approximation where both rings are flat and thin, their inclination angles with respect to the sky plane are respectively 32° and 35°. The gas ring is broader than the dust ring and peaks at smaller distance (typically 87%) to the central stars. The de-projected radial dependence of the line emission displays maxima at $\sim 1.2''$ and $1.9''$ from the central stars, bracketing the mean dust ring radius of $\sim 1.6''$. It cuts-off sharply at a mean distance of $\sim 1''$, cancelling completely below $\sim 0.54''$. Azimuthal rms variations of the dust and gas emissions in the disc planes are measured at the respective levels of $\sim \pm 9\%$ and $\pm 17\%$. Strong evidence is obtained for the rotation of the tilted gas disc about its axis dominating the kinematics.

A detailed study of the properties of the gas disc has been presented, adding significant new contributions to the earlier analysis of Tang et al. (2016). From the azimuthal dependence of the sharpness of the inner edge of the disc, a 95% confidence level upper limit of $0.24''$ (34 au) has been placed on its scale height $H(r)$ at a distance of $1''$ (140 au) from the central stars. At 30 K, hydrostatic equilibrium would imply $H(r)/r \sim 0.17$, consistent with this observation.

Variations of the integrated intensity across the disc area have been studied in detail and found to confirm the presence of a hot spot in the south-eastern quadrant. However several other significant fluctuations, in particular a depression in the northern direction, have also been revealed. On average, the rms relative variation of the integrated intensity reaches only $\sim 17\%$. The radial dependence of the integrated intensity is modulated with enhancements at $r \sim 1.2''$ and $1.9''$, bracketing the dust ring ($\sim 1.6''$). It is also between these radial integrated intensity enhancements that both the hot spot and the northern depression are observed to peak (their effects nearly cancelling each other when averaged over ω).

The study of the gas kinematics has given evidence for a strong dominance of rotation about the disc axis. The Doppler velocity gradient being perpendicular to the projection of the disc axis on the sky plane allows placing a 99% confidence upper limit of 9% on the ratio between a possible in-fall velocity and the rotation velocity. The difficulty of evaluating reliably the rotation velocity close to the sky plane projection of the disc axis has been illustrated and commented upon. Taking this in proper account, the rotation is observed to be Keplerian with a power index of ~ -0.51 across most of the disc area. At $r = 1''$, the rotation velocity reaches $\sim 3.1\,\mathrm{km\,s^{-1}}$, in agreement with the value measured by Dutrey et al. (2014) for ^{12}CO(6–5). No significant anomaly can be revealed in regions of important integrated intensity variation such as the hot spot and the northern depression.

Finally, the dependence of the line width on r and ω has been studied. It shows little dependence on ω and increases as r decreases: the σ of the line, σ_{vz}, increases from $\sim 0.18\,\mathrm{km\,s^{-1}}$ to $\sim 0.26\,\mathrm{km\,s^{-1}}$ when r decreases from $2.3''$ to $1.5''$. As the contributions of Keplerian shear and instrumental spectral resolution taken together should not exceed some $0.11\,\mathrm{km\,s^{-1}}$, a possible explanation may be a factor ~ 2 decrease of the disc surface temperature and opacity, reaching respectively 36 K and 10 at $r = 1.5''$. Relative variations of the line width over the disc area have been found to be strongly correlated with relative variations of the integrated intensity, the former being about a third of the latter. At least qualitatively, this result would also support the presence of a temperature gradient, the CO(3–2) emission ladder peaking at temperatures higher than the average disc temperature.

These new results contribute significant additional information and complement the earlier conclusions reached by Dutrey et al. (2014) and Tang et al. (2016). However, considerations on optical thickness, which are discussed in detail by Tang et al. (2016), are not repeated here. Moreover, interpretations of the observed variations of the integrated intensity as signalling the formation of a planet or of a new companion star remain valid suggestions that would require detailed modelling to be validated. However, this is beyond the scope of the present work.

Acknowledgements This paper makes use of the following ALMA data: ADS/JAO.ALMA#2012.1.00129.S. ALMA is a partnership of ESO (representing its member states), NSF (USA) and NINS (Japan), together with NRC (Canada), NSC and ASIAA (Taiwan), and KASI (Republic of Korea), in cooperation with the Republic of Chile. The Joint ALMA Observatory is operated by ESO, AUI/NRAO and NAOJ. This research has made use of the SIMBAD database, operated at CDS, Strasbourg, France, and of the NASA ADS Abstract

Services. We thank the anonymous referee for useful comments that helped in improving the presentation of this work. We thank the members of the initial "GG Tau team" for early contributions, Jeff Bary, Tracy Beck, Hervé Beust, Yann Boehler, Frederic Gueth, Jean-Marc Huré, Vincent Piétu, Arnaud Piérens and Michal Simon. This research is funded by the Vietnam National Foundation for Science and Technology Development (NAFOSTED) (No. 103.99–2016.50). The Department of Astrophysics (VNSC/VAST) acknowledges support from the World Laboratory, Rencontres du Viet Nam, the Odon Vallet fellowships, Vietnam National Space Center and Graduate University of Science and Technology. Anne Dutrey and Stéphane Guilloteau thank the French CNRS programs PNP, PNPS and PCMI.

References

Di Folco, E., Dutrey, A., Le Bouquin, J.-B., et al. 2014, A&A, 565, L2

Dutrey, A., Di Folco, E., Beck, T., & Guilloteau, S. 2016, A&A Rev., 24, 5

Dutrey, A., Guilloteau, S., & Simon, M. 1994, A&A, 286, 149

Dutrey, A., di Folco, E., Guilloteau, S., et al. 2014, Nature, 514, 600

Piétu, V., Dutrey, A., & Guilloteau, S. 2007, A&A, 467, 163

Tang, Y.-W., Dutrey, A., Guilloteau, S., et al. 2016, ApJ, 820, 19

Teague, R., Guilloteau, S., Semenov, D., et al. 2016, A&A, 592, A49